Light-field ghost imaging

A. Paniate,[1,2,†] G. Massaro,[3,4,†] A. Avella,[2,*] A. Meda,[2] F.V. Pepe,[3,4] M. Genovese,[2]
M. D'Angelo,[3,4,‡] and I. Ruo-Berchera[2,‡]

[1]*DISAT, Politecnico di Torino, Corso Duca degli Abruzzi 24, Torino 10129, Italy*

[2]*Quantum metrology and nano technologies division, INRiM, Strada delle Cacce 91, Torino 10135, Italy*

[3]*Dipartimento Interateneo di Fisica, Università degli Studi di Bari Aldo Moro, Bari 70125, Italy*

[4]*Istituto Nazionale di Fisica Nucleare (INFN), Sezione di Bari, Bari 70125, Italy*

Techniques based on classical and quantum correlations in light beams, such as ghost imaging, allow us to overcome many limitations of conventional imaging and sensing protocols. Despite their advantages, applications of such techniques are often limited in practical scenarios where the position and the longitudinal extension of the target object are unknown. In this work, we propose and experimentally demonstrate an imaging technique, named light-field ghost imaging, that exploits light correlations and light-field imaging principles to enable going beyond the limitations of ghost imaging in a wide range of applications. Notably, our technique removes the requirement to have prior knowledge of the object distance, allowing the possibility of refocusing in postprocessing, as well as performing three-dimensional imaging while retaining all the benefits of ghost imaging protocols.

I. INTRODUCTION

Correlations in light beams have been explored in both quantum and classical contexts to overcome the limitations of conventional optical measurements [1–11] and, in particular, of imaging [12–31]. In the quantum domain, correlation and entanglement have been demonstrated to improve the sensitivity in imaging of amplitude and phase samples [32], enabling real-time sub-shot-noise microscopy [33] and pattern recognition [34]. However, correlation properties relevant to imaging can also be found in specific kinds of classical beams, and many protocols originally developed in the quantum domain have been shown to work regardless of the origin, either quantum or classical, of the correlation [13,16,25,26]. Still, the imaging performances enabled by classical correlations tend to be outperformed by quantum ones, especially in the low photon-number regime [35]; a relevant example is the impossibility of achieving sub-shot-noise sensitivity by means of classical correlations [36–39].

One of the most celebrated techniques that came out in this context is ghost imaging (GI). In GI [12–17], two correlated beams are used: one beam propagates towards a "reference" spatially resolving detector, either freely or through optical elements; the other beam illuminates the object of interest, and a "bucket" detector collects a signal proportional to the *total* intensity of light transmitted, reflected, scattered, or even transduced by the object. The image is not directly formed on the spatially resolving sensor, but is instead reconstructed by correlating the fluctuations of intensities registered by the reference and the bucket detectors. This is possible since the spatial intensity pattern on the object is correlated in space and time with that impinging on the reference detector. In such a scheme, the bucket detector is not meant to detect the accurate spatial distribution of light on the object, and hence no cumbersome optical imaging systems and spatial resolving detectors are needed in the object arm; on the other hand, the propagation of the correlated beam toward the spatially resolving detector can occur through a different optical path in a controlled environment. For this reason, GI is much less sensitive than conventional imaging to detrimental effects connected to the propagation from the object to the sensor. This property makes GI-based protocols particularly interesting when either propagation from the object is heavily disturbed, or the object itself converts the impinging electromagnetic field into a signal of a different nature (e.g., a neuronal pulse). However, a drawback of GI is the need to acquire a large number of frames to

compute the correlations; this makes GI relatively slow compared to imaging techniques based on direct intensity detection. In particular, when the object distance is not known, as one may expect in real applications, it is not possible to adapt focusing in real time: many blurred ghost images would need to be acquired, while tentatively changing the focus plane of the imaging system, till the correct conjugate plane is identified. Of course, increasing the native depth of field is always possible, but this is at the expense of giving up longitudinal resolution. Arguably, this is one of the main reasons why GI and its variants have not yet overcome the barrier to widespread application.

In traditional (not quantum) optics, a direct technique called plenoptic imaging or light-field imaging (LFI) enables the user to reconstruct (or refocus) out-of-focus parts within the acquired image and to change the point of view, in postprocessing [40–42]. This is enabled by the simultaneous detection of the spatial distribution and the propagation direction of light, which is achieved by placing a microlens array (MLA) between the imaging lens and the sensor of a standard imaging device [42–48]. The MLA forms subimages by rays coming from different portions of the imaging lens, thus offering different perspectives on the scene of interest. As a drawback, the spatial resolution is decreased with respect to the diffraction limit, as defined by the numerical aperture of the imaging lens; such resolution loss is, in fact, proportional to the number of directional resolution cells. Still, LFI is one of the simplest and fastest state-of-the-art methods to achieve volumetric images [49–60]. Hence, despite the aforementioned limitation, LFI is increasingly employed in diversified tasks, including 3D imaging and sensing [55,61], stereoscopy [41,62,63], particle image velocimetry [64], particle tracking and sizing [65], wavefront sensing [56,66–68], and microscopy [49,54,56,69]. Recently, an interesting correlation technique, called *correlation plenoptic imaging* (CPI), has been developed, with the specific purpose of improving volumetric resolution with respect to direct LFI methods [70–82]. CPI exploits the simultaneous momentum and position correlation in two classical or quantum beams to obtain, at the same time, high spatial and directional resolution; this is achieved by correlating light intensities measured by two disjoint detectors, each one imaging a different plane, at a different optical distance from the source.

However, both LFI and CPI require that a spatially resolving detector is placed in the object's optical path, and that light propagating from the scene to the sensors behaves in a predictable way, as scattering and distortion effects would hinder the one-to-one correspondence between the image and object point.

In this paper, we show that the principles of LFI and GI can form the basis of a technique called *light-field ghost imaging* (LFGI), which combines the use of a bucket detector, in the object arm, with the availability of

directional information provided by the insertion of an MLA before the spatially resolving sensor. Such a realization represents an adaptation of plenoptic imaging to GI tasks. LFGI shares the benefits of both GI and LFI: its refocusing capabilities enable overcoming the impossibility of standard GI for real-time focusing, and its bucket detection offers increasing robustness to distortion, scattering, and noise in the surrounding object, with respect to direct LFI. Moreover, while extending the depth of field of GI, LFGI preserves the longitudinal resolution, thus enabling imaging and ranging capabilities, as required in diverse applications, from remote sensing to microscopy.

Here, we demonstrate LFGI with thermal correlated beams, but, with the appropriate differences in the optical schemes, LFGI can be used with any kind of correlated light beams, including those formed by entangled photons generated by spontaneous parametric down-conversion. In this case, a significant advantage in terms of signal-to-noise ratio could be eventually achieved in the low illumination regime, as in the case of GI [83]. It is worth underlining the point that different 3D imaging techniques have been developed that exploit multiple single-pixel detectors and computationally generated light patterns and masks [84–95]. The technique we propose here is based on a completely different paradigm, since it exploits only one single-pixel detector in the object arm, and an unknown random pattern naturally generated by the source, either quantum or classical. This considerably simplifies the architecture of the system in the object arm, compared with schemes in which an array of single-pixel detectors is employed, each of them collecting a specific viewpoint on the scene. Moreover, computational imaging techniques cannot exploit the benefit of entangled-photon illumination; in particular, such techniques will be significantly affected by quantum noise when operated towards the single-photon regime.

II. EXPERIMENT AND RESULTS

We implemented a proof-of-principle experiment demonstrating the validity of our LFGI by employing the experimental scheme depicted in Fig. 1. In this setup, we split the speckled beam generated by a so-called pseudothermal source into two classically correlated intensity patterns, with a characteristic spatial speckled structure [96]. One of the correlated beams is sent to the bucket arm. Here, the beam probes the sample and the transmitted light is collected by a bucket detector that provides a signal proportional to the intensity of the total incident light. The other beam is sent to a standard light-field camera [97] that is essentially composed of a lens, an MLA, and a spatially resolving detector (CCD). The plenoptic camera acquires the combination of angular and spatial information that is necessary for the 3D reconstruction of the GI

signal; to this end, each pixel of the reference arm is correlated with the integrated signal from the bucket detector, as rigorously described in Section III below. The working principle is based on the fact that knowing the intensity and momentum of the light in a transverse plane is sufficient to reconstruct the optical field, in a paraxial approximation, at any transverse plane. Thus, intuitively, the process may be represented as a two-step algorithm. In the first step, the complete space-momentum information at the LFI camera is used to reconstruct the patterns of speckles along the propagation axis at different longitudinal distances. In the second step, one correlates the reconstructed speckle patterns with the bucket detector, as done in standard GI; this enables retrieving a 3D reconstruction of the objects in the bucket arm without knowing, *a priori*, their positions along the propagation axis.

A qualitative example of the refocusing capability of LFGI is shown in Fig. 2, where an experimental image of a "4"-shaped sample reconstructed with both LFGI and GI is reported. In this exemplifying result, the sample is placed at different longitudinal distances from the object plane that would give a focused GI, which we refer to as the "GI-on-focus plane."

When the sample is placed in the GI-on-focus plane, i.e., without displacement, GI retrieves the object correctly, and there is no difference between GI and LFGI. On the contrary, for large displacements, GI fails to produce a sharp image: the acquired blurred images lose most of the information about the object. This effect is caused by the loss of correlation between the detected and the probe intensity patterns on the object, due to the different propagation distances. Conversely, thanks to its refocusing ability, LFGI enables one to identify the corresponding pattern that probes the object and thus to retrieve the object details accurately.

A more systematic and quantitative analysis of the quality of the LFGI reconstructions versus standard GI is reported in Fig. 3(a), which shows the resolution achievable as a function of the displacement. The resolution curves are calculated as the minimum distance between the centers of two slits that gives rise to a resolved image with a visibility of 40%. For a comprehensive analysis, LFGI is compared with both the GI characterized by the same minimal resolution of the plenoptic camera, which is set by the dimension of the microlenses (GI microlens limited), and the GI with resolution limited only by the pixel size (GI pixel limited), as it would be without the MLA. The three curves represent the theoretical minimal resolution achievable with LFGI (green line), GI microlens limited (blue line) and GI pixel limited (yellow line). Note that, while the GI-pixel-limited resolution is better near the zero-displacement plane, it approaches the GI-microlens-limited case for a larger displacement and becomes worse than in LFGI for a displacement as small as 20 mm. Experimentally, all the reported GI reconstructions are retrieved as GI-microlens-limited reconstructions in order to avoid changes in the experimental setup that can affect the final results. The range of displacements we tested is limited due
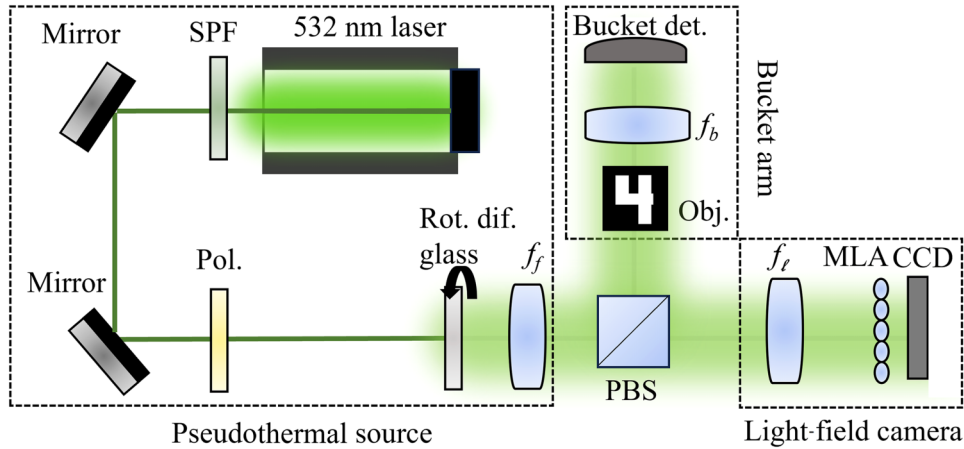

FIG. 1. Schematic of the LFGI: a collimated beam from a cw laser at 532 nm, after being spatially (SPF) and polarization filtered (Pol.), is shone onto a rotating diffusing glass (Arecchi's disk). The scattered light is collected by a far-field lens with focal length $f_f = 75$ mm. The disk and the far-field lens form random speckle patterns at the polarizing beam splitter (PBS). The rotation of the glass generates, in time, different patterns that are equally split by the PBS with a polarization angle of $\pm 45°$ with respect to the axis of the linear polarizer. The speckle pattern has a diameter of 2 cm and each speckle has an averaged transversal size of about 8 μm and an averaged longitudinal length of about 1 mm. One beam is imaged by a light-field camera, composed of a lens with focal length $f_l = 80$ mm and an MLA of dimension 30×30. Each microlens has a focal length $f_{MLA} = 14.6$ mm and a diameter $d = 300$ μm. The MLA is placed at a distance equal to its focal length f_{MLA} from a charge-coupled-device (CCD) camera [Andor Luca R (604)]. The other beam probes the object and is imaged with a lens of focal length $f_b = 75$ mm to a CCD camera (Andor iXon Ultra): the bucket detector is obtained by integrating the signal from all illuminated pixels.
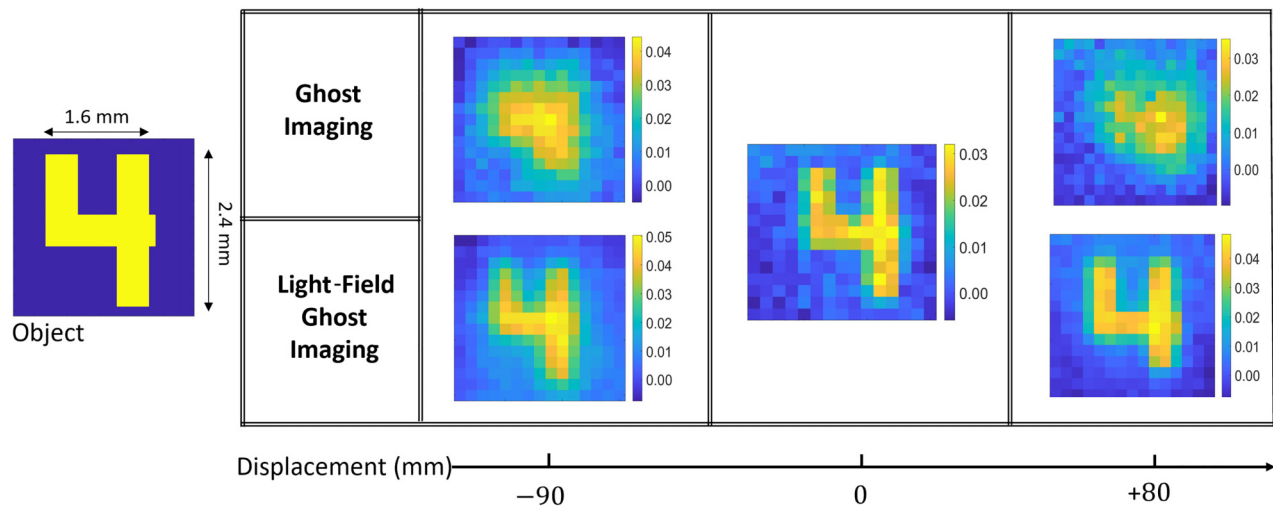
FIG. 2.   Experimental reconstructions of a "4"-shaped sample as a function of displacement. A two-level mask is moved at different displacements from the GI-on-focus plane and the GI and LFGI reconstructions are retrieved. For each displacement, 5×10^4 independent patterns are acquired with an integration time of 15 ms.

to practical constraints in our optical apparatus; however, in principle, the maximum off-focus distance of the object is only limited by the resolution we aim to achieve. Moreover, as shown in Fig. 3(a), the greater the displacement, the greater the advantage over GI schemes.

In our experiment, the LFGI reconstructions are retrieved considering an area of 20×20 pixels behind each microlens. The center of each microlens, with respect to the sensor's pixel array, is calculated as a weighted sum of the light intensity collected by the pixels behind each microlens during a calibration procedure. The values of the microlens centers are then exploited by the algorithm described in Section III below, making a precise alignment between the microlenses and camera unnecessary. The total number of pixels of the reconstructed images is restricted by the total number of microlenses seen by the camera (22×22 pixels); however, all the shown images are finally cropped around a smaller region of interest. The number of microlenses affects both the field of view and the minimum achievable resolution. The pixel size of the reconstructed zero-displacement plane, namely, the GI plane, is basically determined by the ratio between a microlens size and the magnification of the imaging lens, corresponding to 220 µm in our setup. For object planes with non-null displacement, the magnification slightly changes in relation to $\alpha(\delta)$ and $\beta(\delta)$ of Eqs. (19) and (20) (see Section III below).

Different double-slit masks (from NBS 1963A Thorlabs) at different displacements have been used in order to experimentally verify the LFGI advantage. The coordinates of the dots in Fig. 3(a) respectively represent the displacement and slit separation (the distance between the centers of the two slits) used. For example, the dot label as "1" represents a double slit with separation of 0.5 mm, placed

in the GI-on-focus plane, i.e., at zero displacement. The reconstruction of object "1" is shown in the central panel of Fig. 3(b). In this case, the LFGI and GI-microlens-limited reconstructions coincide, and visibility is well above 40%. For the case represented by the "2" dot in panel (a), the GI and LFGI images are shown in the left-hand panel of Fig. 3(b). The image is well reconstructed by LFGI, while the visibility is quite poor for GI, in agreement with the theoretical prediction. In the right-hand panel, we show the results obtained when the displacement and the slit separation are chosen to be on the limit of the 40% visibility curve of LFGI (green line), as represented by points "3" in panel (a), and well below the corresponding GI visibility (yellow and blue lines): the GI reconstruction is completely blurred, while the slits appear well resolved in LFGI. The plenoptic advantage of LFGI over the GI-microlens-limit case is confirmed in terms of resolution for every displacement; with respect to the GI-pixel-limited case, the advantage appears for displacements $\gtrsim 20$ mm due to the loss of resolution introduced by MLA of the LFI camera. Moreover, the enhancement provided by LFGI over GI is not limited to the mere extension of the depth of field of GI, as shown in Fig. 3(a). In fact, the unique feature of LFI is the possibility to refocus on different planes, after the acquisition, without losing longitudinal resolution. LFGI thus provides the depth information of the reconstructed objects, as demonstrated in Fig. 4.

Two single slits, slit_1 and slit_2, are placed at different distances from the PBS, at -80 and $+80$ mm, respectively. The 3D reconstruction of LFGI allows refocusing *a posteriori* on both sets of planes corresponding to slit_1 and to slit_2. In Fig. 4(b), the LFGI reconstructions of the two single slits are reported: in the left picture, we refocused on slit_1 and, as a result, slit_2 is out of focus; in the right
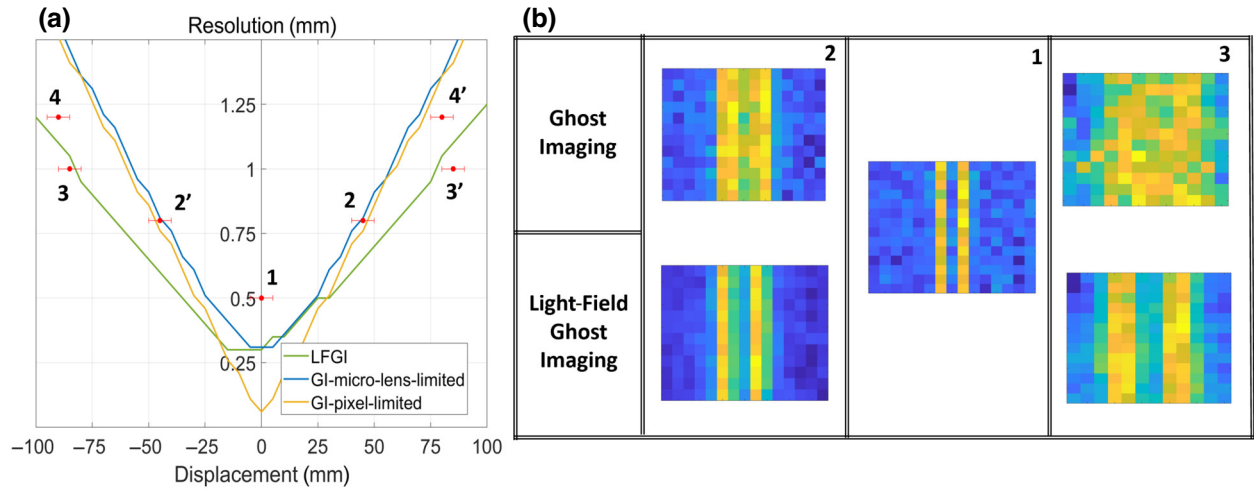
FIG. 3. Resolution of GI and LFGI as a function of the displacement. (a) The curves represent the set of points where the visibility of a double slit is exactly 40% for the GI-microlens-limited, GI-pixel-limited, and LFGI reconstructions, respectively. (b) Examples of GI and LFGI reconstructions of double-slit masks with different separations and different displacements, as indicated by the red circles in (a). The same conclusions can be derived from the other points ("2′," "3′," "4," "4′") that are not reported for brevity. All LFGI reconstructions show visibility greater than or equal to 40%.

picture, we refocused on $slit_2$ and $slit_1$ appears completely blurred. This example shows the sectioning capability of a 3D scene enabled, in postprocessing, by LFGI.

III. METHODS

The information on the reconstructed images is encoded in the plenoptic function

$$P(\mathbf{x}) = \langle (I_B - \langle I_B \rangle)(I(\mathbf{x}) - \langle I(\mathbf{x}) \rangle) \rangle, \qquad (1)$$

obtained by correlating the fluctuations of the intensity I_B acquired by the bucket detector, which is proportional to the total intensity of light that propagates from the object, with the fluctuations of the intensity registered by the pixel centered on the transverse coordinate $\mathbf{x}$ of the reference

sensor. For mitigating the effect of the noisy background typical of thermal light GI, we actually replace I_B with a "differential" signal [35,98].

The conceptual scheme of Fig. 5 provides an intuitive picture of the working principle of LFGI. Here, for convenience, the source of correlated light beams is compressed in the vertical thick orange bar and the two correlated beams are shown on the right and on the left of the source, along in terms of the Klyshko picture [16,99,100]. In this picture, we call *plane b* the plane of the object in the bucket arm and *plane b′* the plane correlated with the object plane in the reference arm. Let us start by considering, in the geometric optics approximation, two explanatory cases. In the first case [Fig. 5(a)], *plane b′* corresponds to the GI-on-focus plane (i.e., the plane whose image, realized
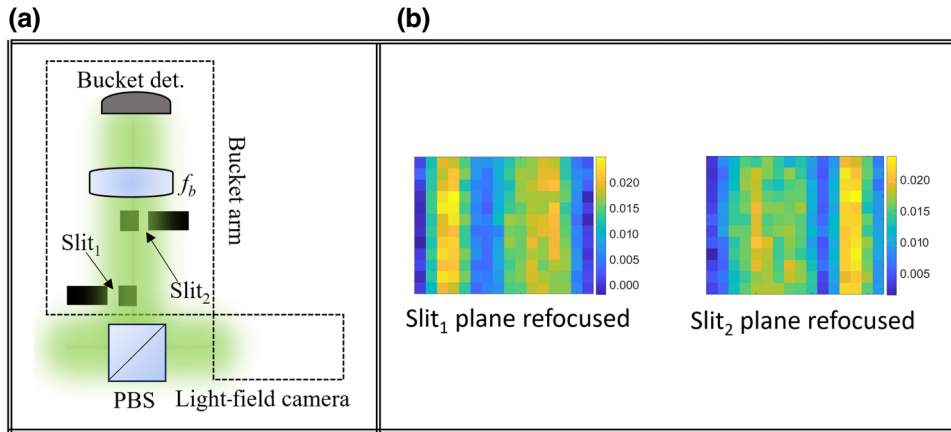

FIG. 4. Refocusing ability of LFGI. (a) Two 1-mm-wide slits ($slit_1$ and $slit_2$) are placed with displacement -80 and $+80$ mm, respectively, in the configuration shown in the figure. (b) In the picture on the left, LFGI is employed to refocus $slit_1$, while $slit_2$ is out of focus; conversely, in the right-hand picture, LFGI refocuses the plane of $slit_2$.
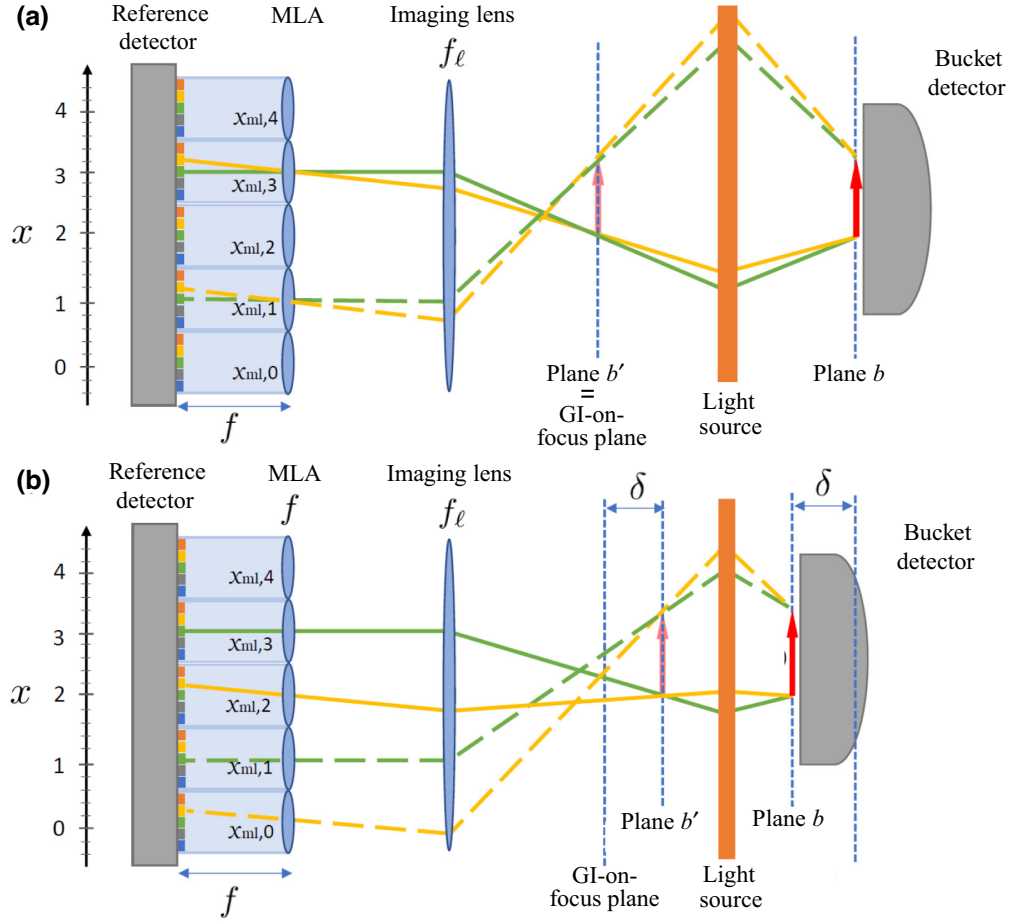
FIG. 5. Schematic representation of the principle of LFGI. Panel (a) shows the scheme when the object is imaged (through correlation measurements) in the zero plane of the light-field camera (i.e., the GI is at focus). Panel (b) shows the scheme when the object is displaced by a distance δ with respect to case (a). The difference between the two cases gives rise to different optical paths for the two pairs of rays emitted by the extreme points of the object. In the focused case, rays emitted by the same object point arrive on the same microlens, regardless of the emission angle. Plenoptic information is irrelevant in this situation. On the contrary, when the ghost image is out of focus, different microlenses are crossed, and specific pixels are illuminated depending on the angle of emission. The quantities and labels appearing in the figure are defined in the text.

by the imaging lens of the light-field camera, is in focus on the plane of the microlenses). Consequently, all rays correlated with a particular point of the object fall on the same microlens. Therefore, in Eq. (1), we can evaluate $I(x)$ by integrating all pixels below each microlens. On the contrary, when there is a displacement δ between *plane b'* and the GI-on-focus plane, as in Fig. 5(b), rays correlated with the same point of the object fall on different microlens. However, the coordinates of the pixels below each microlens identify precisely the light propagation direction, which we represent by a different color in the picture [101]; this allows us to obtain information on the whole 3D light field propagating from the source. The algorithm to obtain $I(x)$ in the more interesting Fig. 5(b) case where displacement is nonzero will now be identified through an accurate analysis of the LFGI scheme.

Because of the statistical properties of the source, the correlation between the intensity fluctuations of Eq. (1)

reduces to

$$P(\mathbf{x}) \simeq \int |\langle E_{\text{ref}}^{*}(\mathbf{x}) E_{B}(\mathbf{x}_b) \rangle|^2 d\mathbf{x}_b, \tag{2}$$

where E_{ref}^{*} and E_B are the electric fields at the reference and bucket detectors, respectively. Without loss of generality, we can put the bucket detector immediately behind the object, so that E_B is also the electric field at the object. Both E_{ref} and E_B can be obtained by respectively propagating the field at planes b' and b through the two optical paths, which gives

$$E_{\text{ref}}(\mathbf{x}) = \int E(\mathbf{x}_b') e^{ik(\mathbf{x}_o - \mathbf{x}_b')^2/2\delta} \mathcal{P}\left(\mathbf{x}_o + \frac{\mathbf{x}_i}{M}\right)$$
$$\times \mathcal{L}(\mathbf{x}, \mathbf{x}_i) d\mathbf{x}_o d\mathbf{x}_i d\mathbf{x}_b', \tag{3}$$

$$E_B(\mathbf{x}_b) = \mathcal{A}(\mathbf{x}_b) \cdot E(\mathbf{x}_b), \tag{4}$$

where $E(x'_b)$ is the speckled electric field at *plane b'*, $e^{ik(\mathbf{x}_o - \mathbf{x}'_b)^2/2\delta}$ is the free propagation between *plane b'* and the GI-on-focus plane, $\mathcal{P}(\mathbf{x})$ is the point-spread function of the imaging system from the GI-on-focus plane to a plane immediately before the MLA, M is its magnification, and $\mathcal{L}(\mathbf{x}, \mathbf{x}_i)$ is the propagation function from the MLA to the detector plane. In our model, the MLA acts as a periodic 2D phase grating with period $2\Delta x_{ml}$ determined by the radius of a single lenslet, equal along the x and y axes; this property allows us to express $\mathcal{L}$ as a linear superposition of the propagation functions $\mathcal{L}_{\mathbf{x}_{ml}}$, each associated with one microlens (see Fig. 5):

$$\mathcal{L}(\mathbf{x}, \mathbf{x}_i) = \sum_{\mathbf{x}_{ml}} \mathcal{L}_{\mathbf{x}_{ml}}(\mathbf{x}, \mathbf{x}_i) = \sum_{\mathbf{x}_{ml}} f_{\mathbf{x}_{ml}}(\mathbf{x}_i) e^{ik(\mathbf{x} - \mathbf{x}_i)^2/2f}. \quad (5)$$

Here f is the microlens focal length, equal throughout the whole array, and

$$f_{\mathbf{x}_{ml}}(\mathbf{x}_i) = \begin{cases} e^{-ik(\mathbf{x}_i - \mathbf{x}_{ml})^2/2f} & \text{if } |\mathbf{x}_i - \mathbf{x}_{ml}|^2 \leq (\Delta x_{ml})^2, \\ 0 & \text{elsewhere} \end{cases}$$
$$(6)$$

is the transmission function of each microlens centered around $\mathbf{x}_{ml}$. In Eq. (4), $\mathcal{A}(\mathbf{x}_b)$ is the object field transmittance, whose square module is reconstructed through refocusing, and $E(\mathbf{x}_b)$ is the speckled electric field impinging on the object. The analytical expression of the plenoptic function is derived by substituting the expressions for E_{ref} and E_B into Eq. (2).

Equations (5) and (6) represent a very general model of the field on the ML plane. This model enables us to take into account the eventual crosstalk, on the sensor, between light from different microlenses. However, in order to actually obtain plenoptic information from $P(\mathbf{x})$, a negligible crosstalk is required. Experimentally, we have employed a light source with a low divergence, which has enabled us to avoid crosstalk between the light *intensity* from neighboring microlenses. By expressing Eq. (3) in terms of Eq. (5), the reference field can be decomposed as a linear superposition:

$$E_{\text{ref}}(\mathbf{x}) = \sum_{\mathbf{x}_{ml}} E_{\mathbf{x}_{ml}}(\mathbf{x}) \quad (7)$$

with

$$E_{\mathbf{x}_{ml}}(\mathbf{x}) = \int E(\mathbf{x}'_b) e^{ik(\mathbf{x}_o - \mathbf{x}'_b)^2/2\delta} \mathcal{P}\left(\mathbf{x}_o + \frac{\mathbf{x}_i}{M}\right)$$
$$\mathcal{L}_{\mathbf{x}_{ml}}(\mathbf{x}, \mathbf{x}_i) d\mathbf{x}_o d\mathbf{x}_i d\mathbf{x}'_b. \quad (8)$$

Hence, the intensity measured on the sensor, which we use as a criterion for assessing crosstalk, has the analytical expression

$$I_{\text{ref}}(\mathbf{x}) = \langle E^*_{\text{ref}}(\mathbf{x}) E_{\text{ref}}(\mathbf{x}) \rangle$$
$$= \sum_{\mathbf{x}_{ml}, \mathbf{x}'_{ml}} \langle E^*_{\mathbf{x}'_{ml}}(\mathbf{x}) E_{\mathbf{x}_{ml}}(\mathbf{x}) \rangle$$
$$= \sum_{\mathbf{x}_{ml}} I_{\mathbf{x}_{ml}}(\mathbf{x}) + 2 \sum_{\mathbf{x}_{ml} \neq \mathbf{x}'_{ml}} \text{Re}[\langle E^*_{\mathbf{x}'_{ml}}(\mathbf{x}) E_{\mathbf{x}_{ml}}(\mathbf{x}) \rangle].$$
$$(9)$$

The formula predicts that the measured reference intensity is a superposition of both the intensities from each microlens, $I_{\mathbf{x}_{ml}}(\mathbf{x}) = \langle E^*_{\mathbf{x}_{ml}}(\mathbf{x}) E_{\mathbf{x}_{ml}}(\mathbf{x}) \rangle$, and interference terms between different microlenses, $\langle E^*_{\mathbf{x}'_{ml}}(\mathbf{x}) E_{\mathbf{x}_{ml}}(\mathbf{x}) \rangle$; the second effect, typically negligible when illumination comes from natural sources, might become relevant for the pseudothermal source employed in our experiment. By imposing the absence of intensity crosstalk, which formally corresponds to requiring that the total intensity is a linear superposition of nonoverlapping envelopes ($I_{\mathbf{x}'_{ml}} I_{\mathbf{x}_{ml}} \simeq 0$), one is also simultaneously ensuring that interference between microlenses can be neglected. Under these conditions, spatially separated nonzero regions can be recognized in $P(\mathbf{x})$, one for each microlens, with analytical expressions

$$P_{\mathbf{x}_{ml}}(\mathbf{x}) \simeq \int |\langle E^*_{\mathbf{x}_{ml}}(\mathbf{x}) E_B(\mathbf{x}_b) \rangle|^2 d\mathbf{x}_b. \quad (10)$$

Hence, the microlens center, $\mathbf{x}_{ml}$, introduces a second variable $\mathbf{x}_{ml}$ on which the plenoptic function depends, under the assumption of no crosstalk; we can thus conveniently adopt the redundant notation $P_{\mathbf{x}_{ml}}(\mathbf{x})$ to indicate the function in Eq. (1), with $\mathbf{x}_{ml}$ representing the center coordinate of the microlens whose image is formed on the pixel in position $\mathbf{x}$. In this way, the plenoptic function becomes explicitly dependent on the expected *four* coordinates.

The plenoptic correlation function can now be conveniently expressed in terms of the two-point correlation function $\langle E^*(\mathbf{x}_b) E(\mathbf{x}'_b) \rangle = \mathcal{S}(\mathbf{x}_b, \mathbf{x}'_b)$, which describes the correlation properties of the speckle patterns at the object ($\mathbf{x}_b$) and ghost image ($\mathbf{x}'_b$) planes, and depends on the experimental properties of the pseudochaotic source and on the object-to-source distance; the result is

$$P_{\mathbf{x}_{ml}}(\mathbf{x}) = \int \left| \int_{S_{ml}} \mathcal{G}(\mathbf{x}_b, \mathbf{x}_i) e^{-ik \mathbf{x}_i \cdot (\mathbf{x} - \mathbf{x}_{ml})/f} d\mathbf{x}_i \right|^2 d\mathbf{x}_b, \quad (11)$$

where

$$\mathcal{G}(\mathbf{x}_b, \mathbf{x}_i) = \int \mathcal{A}^*(\mathbf{x}_b) \mathcal{S}(\mathbf{x}_b, \mathbf{x}'_b) e^{ik(\mathbf{x}_o - \mathbf{x}'_b)^2/2\delta} \mathcal{P}$$
$$\times \left(\mathbf{x}_o + \frac{\mathbf{x}_i}{M}\right) d\mathbf{x}'_b d\mathbf{x}_i \quad (12)$$

is the Green function of conventional (unfocused) GI, and δ is the defocusing distance (displacement from plane o). In fact, the standard ghost image $A_{\mathrm{GI}}(\mathbf{x}_i)$ is obtained as

$$A_{\mathrm{GI}}(\mathbf{x}_i) = \int |\mathcal{G}(\mathbf{x}_b, \mathbf{x}_i)|^2 d\mathbf{x}_b. \qquad (13)$$

The difference between LFGI and conventional GI is easily understood by comparison of Eqs. (13) and (11): whereas the latter is only sensitive to the square module of a given object-dependent quantity $\mathcal{G}$, the former is also sensitive to the modal (directional) content of $\mathcal{G}$; this is due to the fact that the integration over the spatial coordinate $\mathbf{x}_i$ entails a Fourier transformation in the modal coordinate $k(\mathbf{x} - \mathbf{x}_{\mathrm{ml}})/f$ on the sensor plane.

The image of the object, for each defocusing parameter δ, can be expressed by a function R_δ that is obtained from the plenoptic correlation function $P_{\mathbf{x}_{\mathrm{ml}}}$ after the definition of the geometrical correspondence between the coordinates of the object and the coordinates in the reference detector.

According to Eqs. (11) and (12), an object point at coordinate $\mathbf{x}_b$ is mapped on the reference detector as the coordinate pair $(\mathbf{x}_{\mathrm{ml}}, \mathbf{x})$, satisfying the linear relation

$$\mathbf{x}_b = \alpha(\delta)\mathbf{x}_{\mathrm{ml}} + \beta(\delta)\mathbf{x}. \qquad (14)$$

The coefficients $\alpha(\delta)$ and $\beta(\delta)$ are fixed by the defocusing parameter δ. Their full expressions are derived below; in the particular case corresponding to $\delta = 0$ (focused case) they reduce to $\alpha(0) = -1/M$ and $\beta(0) = 0$.

As in conventional light-field imaging, the operation of refocusing requires collecting the signals from all points $(\mathbf{x}_{\mathrm{ml}}, \mathbf{x})$ corresponding (within the approximation entailed by the sensor and microlens array granularity) to the same object point $\mathbf{x}_0$,

$$R_\delta(\mathbf{x}_b) = \sum_{\mathbf{x}} P_{(\mathbf{x}_b - \beta\mathbf{x})/\alpha}(\mathbf{x}), \qquad (15)$$

where α and β are the same δ-dependent coefficients that define the geometrical correspondence of Eq. (14). In Eq. (15), subimages $P_{\mathbf{x}_{\mathrm{ml}}}$ corresponding to a fixed modal coordinate $\mathbf{x}$ are shifted and superimposed, so that each pixel in the final image corresponds to a single coordinate of the object plane.

The correspondence between object points and microlens-angle pairs is obtained through ray tracing. The analysis is easily carried over in a Klyshko picture, tracing rays emitted from the object plane backwards to the source plane, and then forward to the microlenses and reference sensor (see Fig. 5). ABCD matrices are a convenient and compact way to express ray tracing, and will now be used to obtain the final position x_k and angle θ' on the sensor. To this end, we indicate with $M_{\mathrm{lens}}(f)$, $M_{\mathrm{vac}}(z)$, $M_{\mathrm{img}}(o, M)$

the matrices for the propagation of the ray through a lens of focal distance f, a distance z in vacuum, and an imaging system with object distance o and magnification M, respectively, and further introduce

$$M_{\mathrm{src}} = \begin{bmatrix} 1 & 0 \\ 0 & -1 \end{bmatrix} \qquad (16)$$

to describe rays from the source, in the Klyshko picture. If a ray is emitted by the object at position x_b with angle θ and passes through the microlens centered on x_{ml}, its arrival coordinates on the sensor are given by

$$\begin{bmatrix} x_k \\ \theta' \end{bmatrix} = \begin{bmatrix} x_{\mathrm{ml}} \\ 0 \end{bmatrix} + M_{\mathrm{vac}}(f) \cdot M_{\mathrm{lens}}(f)$$
$$\cdot \left(M_{\mathrm{img}}(o, M) \cdot M_{\mathrm{src}} \cdot M_{\mathrm{vac}}(\delta) \begin{bmatrix} x_b \\ \theta \end{bmatrix} - \begin{bmatrix} x_{\mathrm{ml}} \\ 0 \end{bmatrix} \right). \qquad (17)$$

Therefore, by expressing both $x_k(x_b, \theta)$ and $\theta'(x_b, \theta)$ in terms of the plenoptic coordinates x and x_{ml}, a point-to-point correspondence can be obtained between the emission coordinates (x_k, θ) and the coordinates (x_{ml}, x). One way to relate the arrival coordinates and the plenoptic coordinates is

$$x_k(x_b, \theta) = x, \qquad \theta'(x_b, \theta) = (x - x_{\mathrm{ml}})/f, \qquad (18)$$

which can be inverted to recover the object coordinate as a function of the plenoptic coordinates $x_b(x, x_{\mathrm{ml}})$, and the emission angle $\theta(x, x_{\mathrm{ml}})$. The latter represents an irrelevant degree of freedom, which can be neglected, whereas function $x_b(x, x_{\mathrm{ml}})$ is exactly the linear relation anticipated in Eq. (14), with coefficients

$$\alpha(\delta) = -\frac{1}{M}\left(1 + \delta\frac{f_\ell}{M} \right), \qquad (19)$$

$$\beta(\delta) = \delta\frac{M}{f}, \qquad (20)$$

where f_ℓ is the focal length of the imaging lens.

We emphasize that our reconstruction algorithm is based on a scheme where MLA is placed in the imaging plane of the main lens for $\delta = 0$ (see Fig. 5). However, this optical configuration is not mandatory and the reconstruction method could be adapted for a different position of the MLA [81].

IV. CONCLUSIONS

We have proposed and implemented a new correlation imaging scheme, named light-field ghost imaging, that combines the usual advantage of GI (i.e., the use of a single point detector receiving light from the scene of interest

and the intrinsic robustness to distortion and scattering) with the possibility of refocusing, in postprocessing, different planes in the scene. Prior knowledge of the object's distance is thus unnecessary and 3D reconstruction can, in principle, be obtained. This is of the utmost importance since it enables real-time focusing, which is, in general, not possible in correlation imaging, including GI.

This advancement is obtained by measuring on the reference beam, at the same time, the spatial and momentum distributions of light via LFI. The acquisition of complete information on the electromagnetic field allows one to calculate its structure backward till the plane of interest. Remarkably, unlike computational GI [102–105], the proposed technique offers the possibility to reconstruct three-dimensional scenes without any prior knowledge of the intensity patterns on the object; LFGI, in fact, relies only on statistical averages. Such a feature allows one, on the one hand, to exploit fast and uncontrolled sources such as natural ones (see, e.g., Ref. [106]) and, on the other hand, to envisage proper extensions of the LFGI protocol to quantum light.

We stress that one of the difficulties in combining GI and LFI is that the field to be reconstructed is essentially a thermal incoherent field with a limited divergence and a number of transverse wave vectors. This differs from the typical direct LFI scenario, where a scattering object diffuses the light field. In LFGI, the plenoptic camera must be configured for this particular task, and the final 3D capabilities are also related to the speckle features. Interestingly, the interplay between the optical design, the coherence properties of the field at the source (such as speckle size and divergence), and even the influence the absorptive object has on the field divergence give rise to optical performances of LFGI, in out-of-focus planes, that cannot be conveniently expressed in terms of basic optical quantities, as happens in conventional LFI. This dependence deserves to be investigated in depth elsewhere, and it will allow further optimization of the protocol.

Although this work represents a proof of principle of this technique, we believe that LFGI will help to largely extend the range of applicability of GI in remote sensing, including the perspective of faster imaging and ranging applications. Let us note that the principle can also be applied to the spatial characterization of detectors [7,107–109], including depth information, where the surface of the detector can play the role of the "object," and its integrated electric output signal can be correlated with the reference pixel array. In this perspective, LFGI can be helpful for the characterization of quantum technology devices, a field were ghost imaging techniques have already proven to be useful [110,111], and innovative biomedical applications can also be devised. One example is the investigation of the retina's spatial response to light stimuli for the identification of damaged areas or specific pathologies

and exploiting a source with quantum correlations; the technique could also help in investigating the vision process at the single-photon level [112–116].

[1] V. Giovannetti, S. Lloyd, and L. Maccone, Advances in quantum metrology, Nat. Photonics **5**, 222 (2011).

[2] E. Losero, I. Ruo-Berchera, A. Meda, A. Avella, and M. Genovese, Unbiased estimation of an optical loss at the ultimate quantum limit with twin-beams, Sci. Rep. **8**, 7431 (2018).

[3] S. Pradyumna, E. Losero, I. Ruo-Berchera, P. Traina, M. Zucco, C. S. Jacobsen, U. Andersen, I. Degiovanni, M. Genovese, and T. Gehring, Twin beam quantum-enhanced correlated interferometry for testing fundamental physics, Commun. Phys. **3**, 104 (2020).

[4] A. Zavatta, M. D'Angelo, V. Parigi, and M. Bellini, Remote preparation of arbitrary time-encoded single-photon ebits, Phys. Rev. Lett. **96**, 020502 (2006).

[5] T. Iskhakov, A. Allevi, D. Kalashnikov, V. Sala, M. Takeuchi, M. Bondani, and M. Chekhova, Intensity correlations of thermal light: Noise reduction measurements and new ghost imaging protocols, The European Physical Journal Special Topics **199**, 127 (2011).

[6] A. S. Clark, M. Chekhova, J. C. Matthews, J. G. Rarity, and R. F. Oulton, Special topic: Quantum sensing with

correlated light sources, Appl. Phys. Lett. **118,** 060401 (2021).

[7] A. Avella, I. Ruo-Berchera, I. P. Degiovanni, G. Brida, and M. Genovese, Absolute calibration of an EMCCD camera by quantum correlation, linking photon counting to the analog regime, Opt. Lett. **41,** 1841 (2016).

[8] A. Agliati, M. Bondani, A. Andreoni, G. De Cillis, and M. G. A. Paris, Quantum and classical correlations of intense beams of light investigated via joint photodetection, J. Opt. B: Quantum Semiclass. Opt. **7,** S652 (2005).

[9] A. Allevi, S. Olivares, and M. Bondani, Measuring high-order photon-number correlations in experiments with multimode pulsed quantum states, Phys. Rev. A **85,** 063835 (2012).

[10] M. Bondani, A. Allevi, G. Zambra, M. G. A. Paris, and A. Andreoni, Sub-shot-noise photon-number correlation in a mesoscopic twin beam of light, Phys. Rev. A **76,** 013833 (2007).

[11] A. Allevi, S. Olivares, and M. Bondani, High-order photon-number correlations: A resource for characterization and applications of quantum states, Int. J. Quantum Inf. **10,** 1241003 (2012).

[12] T. B. Pittman, Y.-H. Shih, D. V. Strekalov, and A. V. Sergienko, Optical imaging by means of two-photon quantum entanglement, Phys. Rev. A **52,** R3429 (1995).

[13] A. Gatti, E. Brambilla, M. Bache, and L. A. Lugiato, Ghost imaging with thermal light: Comparing entanglement and classical correlation, Phys. Rev. Lett. **93,** 093602 (2004).

[14] M. D'Angelo and Y. Shih, Quantum imaging, Laser Phys. Lett. **2,** 567 (2005).

[15] G. Brida, M. Chekhova, G. Fornaro, M. Genovese, E. Lopaeva, and I. R. Berchera, Systematic analysis of signal-to-noise ratio in bipartite ghost imaging with classical and quantum light, Phys. Rev. A **83,** 063807 (2011).

[16] A. Valencia, G. Scarcelli, M. D'Angelo, and Y. Shih, Two-photon imaging with thermal light, Phys. Rev. Lett. **94,** 063601 (2005).

[17] G. Scarcelli, V. Berardi, and Y. Shih, Can two-photon correlation of chaotic light be considered as correlation of intensity fluctuations?, Phys. Rev. Lett. **96,** 063602 (2006).

[18] M. Genovese, Real applications of quantum imaging, J. Opt. **18,** 073002 (2016).

[19] O. Schwartz, J. M. Levitt, R. Tenne, S. Itzhakov, Z. Deutsch, and D. Oron, Superresolution microscopy with quantum emitters, Nano Lett. **13,** 5832 (2013).

[20] Y. Israel, R. Tenne, D. Oron, and Y. Silberberg, Quantum correlation enhanced super-resolution localization microscopy enabled by a fibre bundle camera, Nat. Commun. **8,** 14786 (2017).

[21] T. Dertinger, R. Colyer, G. Iyer, S. Weiss, and J. Enderlein, Fast, background-free, 3D super-resolution optical fluctuation imaging (SOFI), Proc. Natl. Acad. Sci. **106,** 22287 (2009).

[22] G. B. Lemos, V. Borish, G. D. Cole, S. Ramelow, R. Lapkiewicz, and A. Zeilinger, Quantum imaging with undetected photons, Nature **512,** 409 (2014).

[23] M. D'Angelo, Y.-H. Kim, S. P. Kulik, and Y. Shih, Identifying entanglement using quantum ghost interference and imaging, Phys. Rev. Lett. **92,** 233601 (2004).

[24] G. Scarcelli, Y. Zhou, and Y. Shih, Random delayed-choice quantum eraser via two-photon imaging, The European Physical Journal D **44,** 167 (2007).

[25] R. S. Bennink, S. J. Bentley, and R. W. Boyd, "Two-photon" coincidence imaging with a classical source, Phys. Rev. Lett. **89,** 113601 (2002).

[26] C. Thiel, T. Bastin, J. Martin, E. Solano, J. von Zanthier, and G. S. Agarwal, Quantum imaging with incoherent photons, Phys. Rev. Lett. **99,** 133603 (2007).

[27] T. Ono, R. Okamoto, and S. Takeuchi, An entanglement-enhanced microscope, Nat. Commun. **4,** 2426 (2013).

[28] I. N. Agafonov, M. V. Chekhova, T. S. Iskhakov, and L.-A. Wu, High-visibility intensity interference and ghost imaging with pseudo-thermal light, J. Mod. Opt. **56,** 422 (2009).

[29] A. Meda, A. Caprile, A. Avella, I. Ruo Berchera, I. Degiovanni, A. Magni, and M. Genovese, Magneto-optical imaging technique for hostile environments: The ghost imaging approach, Appl. Phys. Lett. **106,** 262405 (2015).

[30] M. Cassano, M. D'Angelo, A. Garuccio, T. Peng, Y. Shih, and T. V., Spatial interference between pairs of disjoint optical paths with a single chaotic source, Opt. Express **25,** 6589 (2005).

[31] M. D'Angelo, A. Mazzilli, F. Pepe, A. Garuccio, and T. V., Characterization of two distant double-slits by chaotic light secondorder interference, Sci. Rep. **7,** 2247 (2017).

[32] P.-A. Moreau, E. Toninelli, T. Gregory, and M. J. Padgett, Imaging with quantum states of light, Nat. Rev. Phys. **1,** 367 (2019).

[33] N. Samantaray, I. Ruo-Berchera, A. Meda, and M. Genovese, Realization of the first sub-shot-noise wide field microscope, Light Sci. Appl. **6,** e17005 (2017).

[34] G. Ortolano, C. Napoli, C. Harney, S. Pirandola, G. Leonetti, P. Boucher, E. Losero, M. Genovese, and I. Ruo-Berchera, Quantum-enhanced pattern recognition, arXiv:2304.05830 [quant-ph] (2023).

[35] E. Losero, I. Ruo-Berchera, A. Meda, A. Avella, O. Sambataro, and M. Genovese, Quantum differential ghost microscopy, Phys. Rev. A **100,** 063818 (2019).

[36] G. Brida, M. Genovese, A. Meda, and I. Ruo Berchera, Experimental quantum imaging exploiting multimode spatial correlation of twin beams, Phys. Rev. A **83,** 033811 (2011).

[37] D. Gatto Monticone, K. Katamadze, P. Traina, E. Moreva, J. Forneris, I. Ruo-Berchera, P. Olivero, I. P. Degiovanni, G. Brida, and M. Genovese, Beating the Abbe diffraction limit in confocal microscopy via nonclassical photon statistics, Phys. Rev. Lett. **113,** 143602 (2014).

[38] G. Brida, M. Genovese, and I. Ruo-Berchera, Experimental realization of sub-shot-noise quantum imaging, Nat. Photonics **4,** 227 (2010).

[39] E. D. Lopaeva, I. Ruo Berchera, I. P. Degiovanni, S. Olivares, G. Brida, and M. Genovese, Experimental realization of quantum illumination, Phys. Rev. Lett. **110,** 153603 (2013).

[40] G. Lippmann, Épreuves réversibles donnant la sensation du relief, J. Phys. Theor. Appl. **7,** 821 (1908).

[41] E. H. Adelson and J. Y. Wang, Single lens stereo with a plenoptic camera, IEEE Trans. Pattern. Anal. Mach. Intell. **14**, 99 (1992).

[42] R. Ng, M. Levoy, M. Brédif, G. Duval, M. Horowitz, and P. Hanrahan, Light field photography with a hand-held plenoptic camera, Comput. Sci. Techn. Rep. CSTR **2**, 1 (2005).

[43] T. G. Georgiev, A. Lumsdaine, and S. Goma, *High Dynamic Range Image Capture with Plenoptic 2.0 Camera, in Frontiers in Optics 2009/Laser Science XXV/Fall 2009 OSA Optics & Photonics Technical Digest* (Optical Society of America, Washington, DC, 2009), p. SWA7P.

[44] T. G. Georgiev and A. Lumsdaine, Focused plenoptic camera and rendering, J. Electron. Imaging **19**, 021106 (2010).

[45] T. Georgiev and A. Lumsdaine, The multifocus plenoptic camera, in *Digital Photography VIII*, Vol. 8299 (International Society for Optics and Photonics, 2012) p. 829908.

[46] B. Goldlücke, O. Klehm, S. Wanner, and E. Eisemann, Plenoptic cameras, Digital Representations of the Real World: How to Capture, Model, and Render Visual Reality, eds. M. Magnor, O. Grau, O. Sorkine-Hornung, and C. Theobalt (CRC Press, Boca Raton, Florida, USA, 2015).

[47] X. Jin, L. Liu, Y. Chen, and Q. Dai, Point spread function and depth-invariant focal sweep point spread function for plenoptic camera 2.0, Opt. Express **25**, 9947 (2017).

[48] R. Ng, Fourier slice photography, ACM Trans. Graph. **24**, 735 (2005).

[49] M. Levoy, R. Ng, A. Adams, M. Footer, and M. Horowitz, Light field microscopy, ACM Trans. Graph. (TOG) **25**, 924 (2006).

[50] M. Levoy, Z. Zhang, and I. McDowall, Recording and controlling the 4D light field in a microscope using microlens arrays, J. Microsc. **235**, 144 (2009).

[51] A. Cheng, J. T. Gonçalves, P. Golshani, K. Arisaka, and C. Portera-Cailliau, Simultaneous two-photon calcium imaging at different depths with spatiotemporal multiplexing, Nat. Methods **8**, 139 (2011).

[52] S. Abrahamsson, J. Chen, B. Hajj, S. Stallinga, A. Y. Katsov, J. Wisniewski, G. Mizuguchi, P. Soule, F. Mueller, C. D. Darzacq, Xavier Darzacq, Carl Wu, Cornelia I. Bargmann, David A. Agard, Maxime Dahan, and Mats G. L. Gustafsson, Fast multicolor 3D imaging using aberration-corrected multifocus microscopy, Nat. Methods **10**, 60 (2012).

[53] S. Quirin, D. S. Peterka, and R. Yuste, Instantaneous three-dimensional sensing using spatial light modulator illumination with extended depth of field imaging, Opt. Express **21**, 16007 (2013).

[54] M. Broxton, L. Grosenick, S. Yang, N. Cohen, A. Andalman, K. Deisseroth, and M. Levoy, Wave optics theory and 3-D deconvolution for the light field microscope, Opt. Express **21**, 25418 (2013).

[55] X. Xiao, B. Javidi, M. Martinez-Corral, and A. Stern, Advances in three-dimensional integral imaging: Sensing, display, and applications, Appl. Opt. **52**, 546 (2013).

[56] R. Prevedel, Y.-G. Yoon, M. Hoffmann, N. Pak, G. Wetzstein, S. Kato, T. Schrödel, R. Raskar, M. Zimmer, E. S. Boyden, and Alipasha Vaziri, Simultaneous whole-animal 3D imaging of neuronal activity using light-field microscopy, Nat. Methods **11**, 727 (2014).

[57] M. Ren, R. Liu, H. Hong, J. Ren, and G. Xiao, Fast object detection in light field imaging by integrating deep learning with defocusing, Appl. Sci. **7**, 1309 (2017).

[58] D. G. Dansereau, O. Pizarro, and S. B. Williams, Decoding, calibration and rectification for lenselet-based plenoptic cameras, in *Proceedings of the IEEE conference on computer vision and pattern recognition* (IEEE, Portland, OR, USA, 2013), p. 1027.

[59] V. K. Adhikarla, J. Sodnik, P. Szolgay, and G. Jakus, Exploring direct 3D interaction for full horizontal parallax light field displays using leap motion controller, Sensors **15**, 8642 (2015).

[60] S. Wanner and B. Goldluecke, Globally consistent depth labeling of 4D light fields, in *Computer Vision and Pattern Recognition (CVPR), 2012 IEEE Conference on* (IEEE, Providence, Rhode Island, USA, 2012), p. 41.

[61] H.-Y. Liu, E. Jonas, L. Tian, J. Zhong, B. Recht, and L. Waller, 3D imaging in volumetric scattering media using phase-space measurements, Opt. Express **23**, 14461 (2015).

[62] S. Muenzel and J. W. Fleischer, Enhancing layered 3D displays with a lens, Appl. Opt. **52**, D97 (2013).

[63] M. Levoy and P. Hanrahan, Light field rendering, in *Proceedings of the 23rd annual conference on Computer graphics and interactive techniques* (ACM, New Orleans, Louisiana, USA, 1996), p. 31.

[64] T. W. Fahringer, K. P. Lynch, and B. S. Thurow, Volumetric particle image velocimetry with a single plenoptic camera, Meas. Sci. Technol. **26**, 115201 (2015).

[65] E. M. Hall, B. S. Thurow, and D. R. Guildenbecher, Comparison of three-dimensional particle tracking and sizing using plenoptic imaging and digital in-line holography, Appl. Opt. **55**, 6410 (2016).

[66] Y. Lv, R. Wang, H. Ma, X. Zhang, Y. Ning, and X. Xu, SU-G-IeP4-09: Method of human eye aberration measurement using plenoptic camera over large field of view, Med. Phys. **43**, 3679 (2016).

[67] C. Wu, J. Ko, and C. C. Davis, Using a plenoptic sensor to reconstruct vortex phase structures, Opt. Lett. **41**, 3169 (2016).

[68] C. Wu, J. Ko, and C. C. Davis, Imaging through strong turbulence with a light field approach, Opt. Express **24**, 11975 (2016).

[69] W. Glastre, O. Hugon, O. Jacquin, H. G. de Chatellus, and E. Lacot, Demonstration of a plenoptic microscope based on laser optical feedback imaging, Opt. Express **21**, 7294 (2013).

[70] M. D'Angelo, F. V. Pepe, A. Garuccio, and G. Scarcelli, Correlation plenoptic imaging, Phys. Rev. Lett. **116**, 223602 (2016).

[71] F. V. Pepe, F. Di Lena, A. Garuccio, G. Scarcelli, and M. D'Angelo, Correlation plenoptic imaging with entangled photons, Technologies **4**, 17 (2016).

[72] F. V. Pepe, F. Di Lena, A. Mazzilli, E. Edrei, A. Garuccio, G. Scarcelli, and M. D'Angelo, Diffraction-limited plenoptic imaging with correlated light, Phys. Rev. Lett. **119**, 243602 (2017).

[73] F. Di Lena, F. V. Pepe, A. Garuccio, and M. D'Angelo, Correlation plenoptic imaging: An overview, Appl. Sci. **8**, 1958 (2018).

[74] A. Scagliola, F. Di Lena, A. Garuccio, M. D'Angelo, and F. V. Pepe, Correlation plenoptic imaging for microscopy applications, Phys. Lett. A **384,** 126472 (2020).

[75] G. Massaro, D. Giannella, A. Scagliola, F. Di Lena, G. Scarcelli, A. Garuccio, F. V. Pepe, and M. D'Angelo, Light-field microscopy with correlated beams for extended volumetric imaging at the diffraction limit, Sci. Rep. **12,** 16823 (2022).

[76] F. Di Lena, G. Massaro, A. Lupo, A. Garuccio, F. V. Pepe, and M. D'Angelo, Correlation plenoptic imaging between arbitrary planes, Opt. Express **28,** 35857 (2020).

[77] C. Abbattista, L. Amoruso, S. Burri, E. Charbon, Francesco Di. Lena, A. Garuccio, D. Giannella, Z. Hradil, M. Iacobellis, G. Massaro, P. Mos, L. Motka, M. Paúr, Francesco V. Pepe, M. Peterek, I. Petrelli, J. Řeháček, F. Santoro, F. Scattarella, A. Ulku, S. Vasiukov, M. Wayne, C. Bruschini, M. D'Angelo, M. Ieronymaki, and B. Stoklasa, Towards quantum 3D imaging devices, Appl. Sci. **11,** 6414 (2021).

[78] G. Massaro, G. Scala, M. D'Angelo, and F. V. Pepe, Comparative analysis of signal-to-noise ratio in correlation plenoptic imaging architectures, arXiv preprint, arXiv:2206.13412 (2022).

[79] G. Massaro, F. Di Lena, M. D'Angelo, and F. V. Pepe, Effect of finite-sized optical components and pixels on light-field imaging through correlated light, Sensors **22,** 2778 (2022).

[80] F. Scattarella, M. D'Angelo, and F. V. Pepe, Resolution limit of correlation plenoptic imaging between arbitrary planes, Optics **3,** 138 (2022).

[81] G. Massaro, F. V. Pepe, and M. D'Angelo, Refocusing algorithm for correlation plenoptic imaging, Sensors **22,** 6665 (2022).

[82] G. Massaro, P. Mos, S. Vasiukov, F. Di Lena, F. Scattarella, F. V. Pepe, A. Ulku, D. Giannella, E. Charbon, C. Bruschini, and M. D'Angelo, Correlated-photon imaging at 10 volumetric images per second, Sci. Rep. **13,** 12813 (2023).

[83] A. Meda, E. Losero, N. Samantaray, F. Scafirimuto, S. Pradyumna, A. Avella, I. Ruo-Berchera, and M. Genovese, Photon-number correlation for quantum enhanced imaging and sensing, J. Opt. **19,** 094002 (2017).

[84] J. Peng, M. Yao, J. Cheng, Z. Zhang, S. Li, G. Zheng, and J. Zhong, Micro-tomography via single-pixel imaging, Opt. Express **26,** 31094 (2018).

[85] M. Yao, J. Cheng, Z. Huang, Z. Zhang, S. Li, J. Peng, and J. Zhong, Reflection light-field microscope with a digitally tunable aperture by single-pixel imaging, Opt. Express **27,** 33040 (2019).

[86] M. Edgar, G. Gibson, and M. Padgett, Principles and prospects for single-pixel imaging, Nat. Photon **13,** 13 (2019).

[87] M.-J. Sun and J.-M. Zhang, Single-pixel imaging and its application in three-dimensional reconstruction: A brief review, Sensors **19,** 732 (2019).

[88] B. Sun, M. P. Edgar, R. Bowman, L. E. Vittert, S. Welsh, A. Bowman, and M. J. Padgett, 3D computational imaging with single-pixel detectors, Science **340,** 844 (2013).

[89] G. A. Howland, P. B. Dixon, and J. C. Howell, Photon-counting compressive sensing laser radar for 3D imaging, Appl. Opt. **50,** 5917 (2011).

[90] Z. Zhang, S. Liu, J. Peng, M. Yao, G. Zheng, and J. Zhong, Simultaneous spatial, spectral, and 3D compressive imaging via efficient Fourier single-pixel measurements, Optica **5,** 315 (2018).

[91] G. M. Gibson, S. D. Johnson, and M. J. Padgett, Single-pixel imaging 12 years on: A review, Opt. Express **28,** 28190 (2020).

[92] Y. Zhang, M. P. Edgar, B. Sun, N. Radwell, G. M. Gibson, and M. J. Padgett, 3D single-pixel video, J. Opt. **18,** 035203 (2016).

[93] G. A. Howland, D. J. Lum, M. R. Ware, and J. C. Howell, Photon counting compressive depth mapping, Opt. Express **21,** 23822 (2013).

[94] M.-J. Sun, M. P. Edgar, D. B. Phillips, G. M. Gibson, and M. J. Padgett, Improving the signal-to-noise ratio of single-pixel imaging using digital microscanning, Opt. Express **24,** 10476 (2016).

[95] Z. Zhang and J. Zhong, Three-dimensional single-pixel imaging with far fewer measurements than effective image pixels, Opt. Lett. **41,** 2497 (2016).

[96] A. Gatti, D. Magatti, and F. Ferri, Three-dimensional coherence of light speckles: Theory, Phys. Rev. A **78,** 063806 (2008).

[97] C. Hahne, A. Aggoun, S. Haxha, V. Velisavljevic, and J. C. J. Fernández, Light field geometry of a standard plenoptic camera, Opt. Express **22,** 26659 (2014).

[98] F. Ferri, D. Magatti, L. Lugiato, and A. Gatti, Differential ghost imaging, Phys. Rev. Lett. **104,** 253603 (2010).

[99] D. Klyshko, A simple method of preparing pure states of an optical field, of implementing the Einstein–Podolsky–Rosen experiment, and of demonstrating the complementarity principle, Sov. Phys. Usp. **31,** 74 (1988).

[100] R. S. Aspden, D. S. Tasca, A. Forbes, R. W. Boyd, and M. J. Padgett, Experimental demonstration of Klyshko's advanced-wave picture using a coincidence-count based, camera-enabled imaging system, J. Mod. Opt. **61,** 547 (2014).

[101] C. Hahne, A. Aggoun, V. Velisavljevic, S. Fiebig, and P. Matthias, Refocusing distance of a standard plenoptic camera, Opt. Express **24,** 21521 (2016).

[102] Y. Bromberg, O. Katz, and Y. Silberberg, Ghost imaging with a single detector, Phys. Rev. A **79,** 053840 (2009).

[103] J. H. Shapiro, Computational ghost imaging, Phys. Rev. A **78,** 061802 (2008).

[104] B. Sun, M. P. Edgar, R. Bowman, L. E. Vittert, S. Welsh, A. Bowman, and M. J. Padgett, 3D computational imaging with single-pixel detectors, Science **340,** 844 (2013).

[105] Z.-H. Xu, W. Chen, J. Penuelas, M. Padgett, and M.-J. Sun, 1000 fps computational ghost imaging using LED-based structured illumination, Opt. Express **26,** 2427 (0000).

[106] X.-F. Liu, X.-H. Chen, X.-R. Yao, W.-K. Yu, G.-J. Zhai, and L.-A. Wu, Lensless ghost imaging with sunlight, Opt. Lett. **39,** 2314 (2014).

[107] A. Avella, G. Brida, I. Degiovanni, M. Genovese, M. Gramegna, L. Lolli, E. Monticone, C. Portesi, M. Rajteri, M. Rastello, E. Taralli, P. Traina, and M. White, Self consistent, absolute calibration technique for photon number resolving detectors, Opt. Express **19,** 23249 (2011).

[108] M. G. M. L. R. M. C. Giorgio Brida, Marco Genovese, and L. Krivitsky, Single-photon detector calibration by means of conditional polarization rotation, J. Opt. Soc. Am. B **22**, 488 (2005).

[109] G. Brida, M. Genovese, and M. Gramegna, Twin-photon techniques for photo-detector calibration, Laser Phys. Lett. **3**, 115 (2006).

[110] J. Wu, F.-X. Wang, W. Chen, Z.-Q. Yin, S. Wang, Z.-G. Wang, S.-H. Lan, and Z.-F. Han, General temporal ghost imaging model with detection resolution and noise, Appl. Opt. **62**, 1175 (2023).

[111] F.-X. Wang, J. Wu, W. Chen, S. Wang, D.-Y. He, Z. Yin, C. Zou, G. Guo, and Z. Han, Perceiving quantum hacking for quantum key distribution using temporal ghost imaging, Phys. Rev. Appl. **15**, 034051 (2021).

[112] F. Rieke and D. A. Baylor, Single-photon detection by rod cells of the retina, Rev. Mod. Phys. **70**, 1027 (1998).

[113] J. N. Tinsley, M. I. Molodtsov, R. Prevedel, D. Wartmann, J. Espigulé-Pons, M. Lauwers, and A. Vaziri, Direct detection of a single photon by humans, Nat. Commun. **7**, 12172 (2016).

[114] G. D. Field and A. P. Sampath, Behavioural and physiological limits to vision in mammals, Phil. Trans. R. Soc. B **372**, 20160072 (2017).

[115] A. Kelber, C. Yovanovich, and P. Olsson, Thresholds and noise limitations of colour vision in dim light, Phil. Trans. R. Soc. B **372**, 20160065 (2017).

[116] N. Sim, M. F. Cheng, D. Bessarab, C. M. Jones, and L. A. Krivitsky, Measurement of photon statistics with live photoreceptor cells, Laser Phys. Lett. **109**, 113601 (2012).